

## Space debris tracking based on fuzzy running Gaussian average adaptive particle filter track-before-detect algorithm

Peerapong Torteeka<sup>1,2</sup>, Peng-Qi Gao<sup>1</sup>, Ming Shen<sup>1</sup>, Xiao-Zhang Guo<sup>1</sup>, Da-Tao Yang<sup>1</sup>, Huan-Huan Yu<sup>1,2</sup>, Wei-Ping Zhou<sup>1,2</sup> and You Zhao<sup>1</sup>

<sup>1</sup> National Astronomical Observatories, Chinese Academy of Sciences, Beijing 100012, China; [youzhao@bao.ac.cn](mailto:youzhao@bao.ac.cn)

<sup>2</sup> University of Chinese Academy of Sciences, Beijing 100049, China

Received 2016 June 12; accepted 2016 October 25

**Abstract** Although tracking with a passive optical telescope is a powerful technique for space debris observation, it is limited by its sensitivity to dynamic background noise. Traditionally, in the field of astronomy, static background subtraction based on a median image technique has been used to extract moving space objects prior to the tracking operation, as this is computationally efficient. The main disadvantage of this technique is that it is not robust to variable illumination conditions. In this article, we propose an approach for tracking small and dim space debris in the context of a dynamic background via one of the optical telescopes that is part of the space surveillance network project, named the Asia-Pacific ground-based Optical Space Observation System or APOSOS. The approach combines a fuzzy running Gaussian average for robust moving-object extraction with dim-target tracking using a particle-filter-based track-before-detect method. The performance of the proposed algorithm is experimentally evaluated, and the results show that the scheme achieves a satisfactory level of accuracy for space debris tracking.

**Key words:** astrometry — space debris — atmospheric effects — image processing

### 1 INTRODUCTION

Almost 60 years of human space activities, including an unexpected in-orbit collision, have resulted in immense amounts of space debris joining the population of resident space objects (RSOs). Although most space debris larger than 10 cm in diameter have been cataloged, orbit perturbations can disturb the positions of these space objects. Therefore, the six orbital parameters of each RSO should be periodically updated. Currently, ground-based passive optical telescopes are an efficient system that can employ powerful image processing techniques. However, all long-range passive optical observations are not robust under variable illumination conditions (e.g., atmospheric effects and cosmic rays). These conditions cause dynamic backgrounds and light scattering in high-altitude orbits. Thus, space objects appear dim, with a low signal-to-noise ratio (SNR) of less than 10 dB, and are thus difficult to detect. Recently, an optical flow algorithm and a combination of a convolution mask with a Kalman filter have been developed to alleviate this phenomenon (Fujita et al. 2012; Ye & Zhou 2015); however,

they only work well under static and/or Gaussian background noise. Thus, atmospheric effects pose a significant problem. Moreover, moving targets must be sufficiently bright for extraction. To address the above issues, in this article, we propose an approach that combines a robust extraction and tracking method for small and dim space debris under dynamic and/or non-Gaussian backgrounds based on the particle filter track-before-detect algorithm (PF-TBD).

We focus on real-time space debris tracking in a sequence of images based on the leap-frog tracking mode (Hampf et al. 2014). It is known that the principle of conventional particle filters (PFs) is based on the sequential Monte Carlo (SMC) method. The key idea of a conventional PF is to represent the required posterior density function by a set of random samples (particles) with associated weights and to compute estimated values based on these samples and weights. In detail, conventional PFs involve two main procedures: the first is the generation of a sequential sampling based on SMC, and the second is a re-sampling process. Both procedures are fun-

damental for improving PF and developing the next generation of PFs. PF-TBD is an updated version of a PF proposed by Salmond & Birch (2001). Currently, PF-TBD is primarily applied in military missions such as radio detection and ranging applications (Gao & Li 2014). The main difference between a conventional PF and PF-TBD can be described as follows. First, PF-TBD is a type of multiple-model PF that performs non-linear filtering with dynamic models having two conditions (presence of target or absence of target) based on a two-state Markov chain. However, a conventional PF considers only one condition, which is the continuous appearance of the target in time; this condition is extracted by thresholding the output of the signal-processing unit of a sensor. Second, PF-TBD was developed for small and dim targets such as long-range airplanes and ballistic missiles. In most tracking systems, the target state typically consists of kinematic components such as position, velocity and acceleration. However, tracking with PF-TBD usually includes other attributes of the target, such as the intensity value. This is an advantage of PF-TBD as the algorithm can track targets with low SNR and without a threshold. However, an astronomical background includes space debris, fixed stars and disturbance noise. Over short periods of time, moving space debris and fixed stars have a similar appearance in terms of the point spread function (PSF), because the conventional PF-TBD cannot distinguish between objects that have similar patterns. Such objects should first be processed using a moving object extraction algorithm, such as a combined median image subtraction and tracking approach (Stoveken & Schildknecht 2005) or extraction with mathematical morphology (Sun & Zhao 2013). Both techniques are widely used in the field of astronomy to recognize moving space debris before the tracking process. However, they only work well under static and Gaussian backgrounds. To overcome this limitation, we propose a method that combines moving object extraction based on a running Gaussian average (RGA) (Ng & Delp 2010), adapted from the fuzzy logic algorithm (RGA-Fuzzy), with PF-TBD as illustrated by the system diagram of the proposed method shown in Figure 1.

We automatically optimize the dynamics of the astronomical background model under the intelligent fuzzy conditions (Raol 2009) shown in Figure 2, which describe the membership functions as well as their boundary of the fuzzy set and fuzzy inference table, in order to design a fuzzy automatic adjustment model.

The remainder of this work is organized as follows. Section 2 discusses some background aspects of RGA-Fuzzy that are used to develop the robust extraction and

tracking scheme for real-time space debris observations. Section 3 presents specifications of the APOSOS telescope, the astronomical image datasets for validation and some experimental results. Finally, Section 4 concludes this article.

## 2 METHODOLOGY

### 2.1 RGA-Fuzzy for Moving Space Debris Extraction

The computer vision technique of RGA is the updated version of static background subtraction, and has been widely used in the initial stages of moving object detection and tracking. However, in real environments, static background subtraction does not perform well on dynamic backgrounds. The basic RGA process can be expressed as follows

$$\delta_N^{(x,y)} = \frac{1}{N} \sum_{k=1}^N I_k^{(x,y)}, \quad (1)$$

where  $N$  is the number of frames used to construct the astronomical background model ( $\delta_N^{(x,y)}$ ) in two-dimensional (2D) spatial coordinates  $(x, y)$ , and  $I_k^{(x,y)}$  is the intensity of the present image ordered by  $k \in \mathbb{R}^+$ . After  $\delta_N^{(x,y)}$  has been constructed, we can calculate the absolute difference image ( $D_t^{(x,y)}$ ) between  $\delta_t^{(x,y)}$  and  $I_t^{(x,y)}$  at time ( $t$ ). We modify the new optimal  $\delta_t^{(x,y)}$  using the empirical weight ( $\alpha \in [0, 1]$ ), which depends on the scene variability. In traditional RGA, the intensity level of  $D_t^{(x,y)}$  can be described by three cases based on two boundary thresholds, the upper limit ( $\tau_{up}$ ) and lower limit ( $\tau_w$ ). This can be written as follows

$$\delta_t^{(x,y)} = \begin{cases} \delta_{t-1}^{(x,y)} & \text{if } D_t^{(x,y)} \geq \tau_{up} \\ \alpha I_t^{(x,y)} + (1 - \alpha) \delta_{t-1}^{(x,y)} & \text{if } \tau_w \leq D_t^{(x,y)} \leq \tau_{up} \\ I_t^{(x,y)} & \text{if } D_t^{(x,y)} \leq \tau_w \end{cases} \quad (2)$$

Typically,  $\alpha$  is manually adjusted according to human visual interpretation; it can be observed from the scene variability. This process is complicated and readjustments are time-intensive. To overcome this limitation, a Mamdani-type fuzzy logic (MFL) was designed to automatically adjust  $\alpha$  based on Equation (2) with two input parameters: the intensity level of  $D_t^{(x,y)}$  and the input image signal-to-clutter ratio ( $SCR_i$ ) (Wang & Qin 2015). Normally, the image SCR value represents the performance of small-target extraction, which can be defined as  $SCR = |\mu_{ob} - \mu_{bk}| / \sigma_{bk}^{ROI}$ , where  $\mu_{ob}$  is the average intensity of the object of interest,  $\mu_{bk}$  is the average of the background intensity and  $\sigma_{bk}^{ROI}$  is the standard deviation (STD) of background intensity within the specified

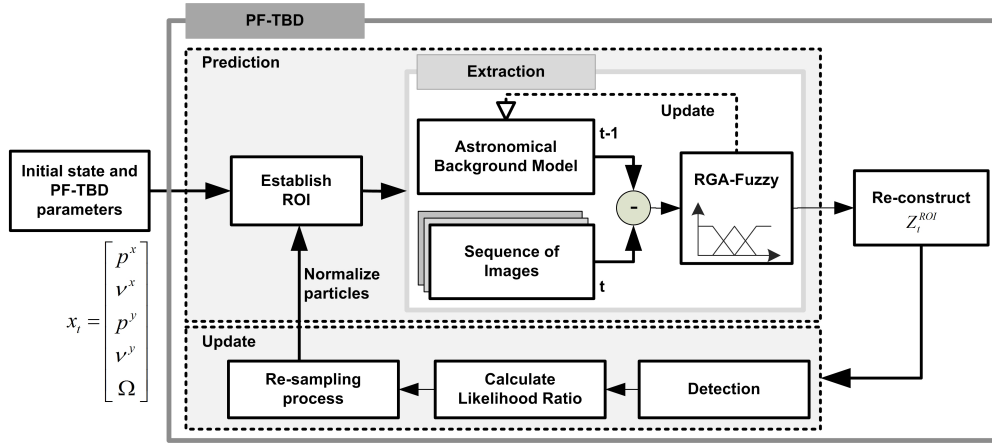


Fig. 1 System diagram of the proposed RGA-Fuzzy adaptive PF-TBD algorithm for tracking small and dim space debris.

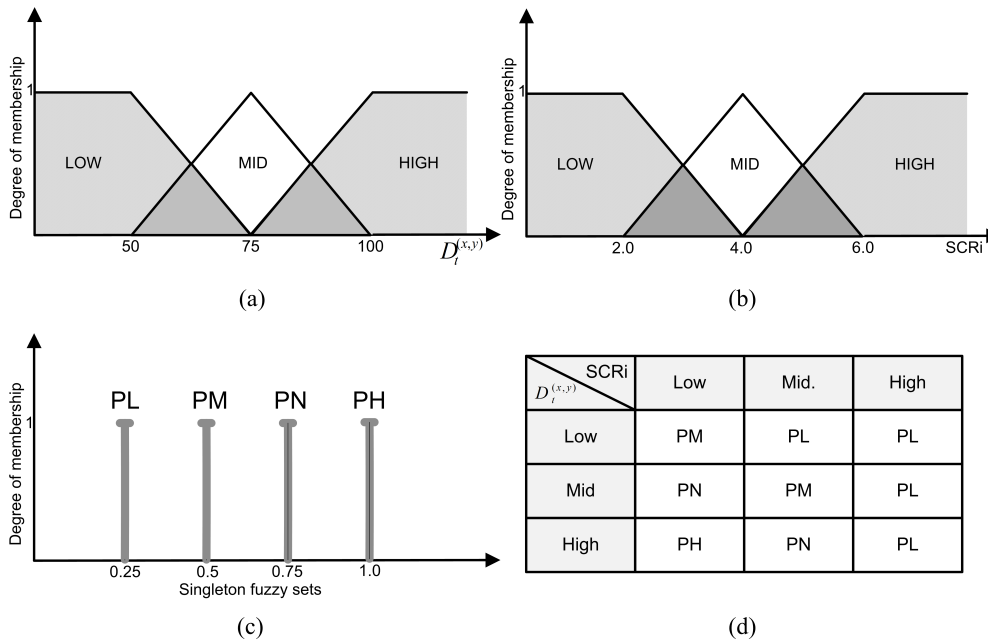


Fig. 2 (a) Membership functions of  $D_t^{(x,y)}$  with  $\tau_{up} = 100$  and  $\tau_w = 50$ ; (b) membership function of  $SCR_i$  with range  $[0, 6]$ ; (c) singleton fuzzy sets; and (d) fuzzy inference table.

region of interest (ROI), which excludes the object region.

Further advances in the development of MFL will require three main tasks to be accomplished. First, the fuzzification procedure converts the crisp value of the two input parameters into the three dimensions of the fuzzy set with triangle-shaped membership functions. These are linguistically defined as low, mid and high, as shown in Figure 2(a)–(b). Next, the results of the fuzzification procedure are associated with singleton fuzzy sets named positive low (PL), positive medium (PM), positive normal (PN) and positive high (PH). These are based on

the AND operation, which we refer to as the inference fuzzy procedure, as shown in Figure 2(c)–(d). Finally, the centroid defuzzification step is performed. This converts the results in the fuzzy domain into a crisp value, i.e., the optimal value of  $\alpha$ , by re-adjusting the recursive function in Equation (2) without any burden on, or bias from, a human.

## 2.2 RGA-Fuzzy Adaptive PF-TBD for Robust Space Debris Tracking

In this study, we combined RGA-Fuzzy within the tracking loop to improve the measurement data, as shown

in Figure 1. In the case of tracking a single dim piece of space debris, PF-TBD is a state-estimation method that incorporates prediction and updating stages. In the prediction stage, the kinematic model of moving space debris on the celestial sphere projected to a 2D spatial coordinate can be defined by the state vector  $x_t = [p^x, v^x, p^y, v^y, \Omega]^T$ , where  $(p^x, p^y)_t$ ,  $(v^x, v^y)_t$  and  $\Omega_t$

are the position, velocity and intensity level of the space debris, respectively. The propagation of state variables occurs according to a linear state transition matrix ( $A_t$ ), which is a time invariant system with sampling interval ( $T$ ). This can be defined in terms of the state vector using the linear stochastic equation

$$x_{t+1} = A_t x_t + w_t, \quad E_t \in \{e, \bar{e}\}. \quad (3)$$

Hence,

$$A_t = \begin{bmatrix} 1 & T & 0 & 0 & 0 \\ 0 & 1 & 0 & 0 & 0 \\ 0 & 0 & 1 & T & 0 \\ 0 & 0 & 0 & 1 & 0 \\ 0 & 0 & 0 & 0 & 1 \end{bmatrix}, \quad Q_t = \begin{bmatrix} \frac{\varphi_1}{3}T^3 & \frac{\varphi_1}{2}T^2 & 0 & 0 & 0 \\ \frac{\varphi_1}{2}T^2 & \varphi_1 T & 0 & 0 & 0 \\ 0 & 0 & \frac{\varphi_2}{3}T^3 & \frac{\varphi_2}{2}T^2 & 0 \\ 0 & 0 & \frac{\varphi_2}{2}T^2 & \varphi_2 T & 0 \\ 0 & 0 & 0 & 0 & \varphi_2 T \end{bmatrix},$$

where  $w_t$  is white Gaussian process noise with mean zero and covariance matrix  $Q_t$ . The variances of the target acceleration and return intensity noise are represented as  $\varphi_1$  and  $\varphi_2$ , respectively. The two situations of target ( $E_t$ ) consist of existence ( $e$ ) and non-existence ( $\bar{e}$ ), which are described by the two-state Markov chain in the discrete-time domain (Karlin et al. 1998). In theory, the two-state Markov chain model is a stochastic process for which the probability of entering a certain state ( $t$ ) depends only on the last occupied state ( $t - 1$ ) and not on any earlier state. This is performed by a regime transition (RT) process (Ristic et al. 2004), which transfers the state sequence through a square matrix named transition probability matrix ( $\Pi$ ) having all entries non-negative and all column sums equal to 1.  $\Pi$  can be expressed as follows

$$\Pi = \begin{pmatrix} 1 - P_b & P_b \\ P_d & 1 - P_d \end{pmatrix}, \quad (4)$$

where  $P_b = P(E_t = e | E_{t-1} = \bar{e})$  is the probability of target birth. The probability of target death is  $P_d = P(E_t = \bar{e} | E_{t-1} = e)$ . The measurement model ( $z_t^{(i,j)}$ ) for moving space debris at each time interval consists of two conditions, which can be expressed as

$$z_t^{(i,j)} = \begin{cases} h_t^{(i,j)}(x_t) + y_t, & E_t = e, \\ y_t, & E_t = \bar{e}, \end{cases} \quad (5)$$

where  $h_t^{(i,j)}(x_t)$  is the distribution intensity of space debris in each set of observation cells  $\mathcal{O}_i(x_t)$  and  $\mathcal{O}_j(x_t)$ , as indexed by  $i, j$ , and  $y_t$  is the measurement noise in each cell. We assume that  $y_t$  is independent of  $w_t$  and has a white Gaussian distribution with zero mean and variance  $\varepsilon^2$ .

In this study, the distribution intensity of space debris can be modeled by the PSF as a point target intensity at the rectangular position  $(p^x, p^y)$ . Therefore,  $h_t^{(i,j)}(x_t)$  can be defined as follows

$$h_t^{(i,j)}(x_t) = \frac{\Delta_x \Delta_y \Omega_t}{2\pi \Sigma^2} \exp\left(-\frac{(p_t^x - i\Delta_x)^2 + (p_t^y - j\Delta_y)^2}{2\Sigma^2}\right), \quad (6)$$

where  $\Delta_x$  and  $\Delta_y$  are the sizes of  $\mathcal{O}_i(x_t)$  and  $\mathcal{O}_j(x_t)$  respectively in 2D spatial coordinates. The variable  $\Sigma$  represents the blurring coefficient of the PSF. The likelihood functions of the target in the two situations are the probability density function (pdf) of background noise for each cell  $p(z_t^{(i,j)} | E_t = \bar{e})$  and the pdf of target existence in noise  $p(z_t^{(i,j)} | x_t, E_t = e)$ . These expressions consider the target state  $x_t$  to be based on the assumption of Gaussian measurement noise, which is independent of pixel measurement. The two pdfs can be expressed as follows:

$$p(z_t^{(i,j)} | E_t = \bar{e}) \triangleq \mathcal{N}(z^{(i,j)}, 0, \varepsilon^2) = \frac{1}{\sqrt{2\pi\varepsilon^2}} \exp\left(-\frac{(z_t^{(i,j)})^2}{2\varepsilon^2}\right);$$

$$p(z_t^{(i,j)} | x_t, E_t = e) \triangleq \mathcal{N}(z^{(i,j)}, h_t^{(i,j)}(x_t), \varepsilon^2) = \frac{1}{\sqrt{2\pi\varepsilon^2}} \exp\left(-\frac{(z_t^{(i,j)} - h_t^{(i,j)}(x_t))^2}{2\varepsilon^2}\right).$$

In case of target existence,  $p(z_t^{(i,j)}|x_t, E_t = e)$  will affect only the set of pixels around the target position  $(p^x, p^y)$ , and the expression for this case can be estimated as follows

$$p(z_t^{(i,j)}|x_t, E_t = e) \approx \prod_{i \in \mathcal{O}_i(x_t)} \prod_{j \in \mathcal{O}_j(x_t)} p(z_t^{(i,j)}|x_t, E_t = e) \prod_{i \notin \mathcal{O}_i(x_t)} \prod_{j \notin \mathcal{O}_j(x_t)} p(z_t^{(i,j)}|, E_t = \bar{e}).$$

Thus, the likelihood ratio for each cell is defined as follows

$$\ell(z_t^{(i,j)}|, E_t) = \begin{cases} \frac{p(z_t^{(i,j)}|x_t, E_t = e)}{p(z_t^{(i,j)}|, E_t = \bar{e})}, & E_t = e, \\ 1, & E_t = \bar{e}. \end{cases} \quad (7)$$

From Equation (7), the likelihood function of target existence is given as

$$\ell(z_t^{(i,j)}|x_t, E_t = e) = \prod_{i=1}^{n_l} \prod_{j=1}^{n_c} \exp\left(-\frac{h_t^{(i,j)}(x_t)[h_t^{(i,j)}(x_t) - 2z_t^{(i,j)}]}{2\varepsilon^2}\right). \quad (8)$$

The variables  $n_l$  and  $n_c$  are the number of pixels in the observation cells, which are affected by the space debris intensity. The main steps are summarized as follows: **Algorithm 1:** The proposed combination RGA-Fuzzy and PF-TBD algorithm

**Data:** Sequence of astronomical images, location of telescope and pointing direction, and Tycho-2 star catalog.

**Result:** Vector of state variables  $\bar{x}_t$ .

**Initialization:** At epoch  $(t) = 0$ , initialize the parameters of PF-TBD, i.e., the number of particles ( $n_p$ ),  $T = 1.0$  s,  $\varphi_1 = 0.001$ ,  $\varphi_2 = 0.01$ ,  $\varepsilon^2 = 3.0$ ,  $\Sigma = 0.7$ ,  $P_d = P_b = 0.01$  and  $x_{(t=0)}$ .

**while** *index* ( $i$ ) = 1 : 1 : length of the track ( $L$ ) **do**

**Step 1.** The target existence transitions. In the space debris scenario, the prediction for each particle's existence  $E_t^n$ ,  $n = 1, \dots, n_p$  is performed using a two-state Markov chain model based on the RT:  $[\{E_t^n\}]_{n=1}^{n_p} = \text{RT}[[\{E_{t-1}^n\}]_{n=1}^{n_p}, \Pi]$ .

**Step 2.** FOR  $i = 1 : n_p$  DO,

Generate a set of particles based on the uniform proposal density function ( $\rho$ ). Then,

- For the set of target newborn particles:  
( $E_t^n = e, E_{t-1}^n = \bar{e}, z_t$ ), build  $x_t^n \sim \rho(x_t^n | z_t)$ .
- For the set of target survival particles:  
( $E_t^n = e, E_{t-1}^n = e, z_t$ ), build  $x_t^n \sim \rho(x_t | x_{t-1}^n, z_t)$  based on Equation (3).
- Average the position of the prediction state, and then establish a specific ROI of size  $64 \times 64$  pixels<sup>2</sup> from  $\hat{x}_p = 1/n_p \sum_{n=1}^{n_p} \rho(p^x, p^y | z_t)$ .

**Step 3.** Reconstruct the sequence of real measurement data ( $\tilde{z}_t$ ) by duplicating the optimal image from RGA-Fuzzy.  $[\{\tilde{z}_t\}] = \text{RGA-Fuzzy}[z_t^{\text{ROI}}, \delta_t^{\text{ROI}}]$ .

**Step 4.** Use this to evaluate  $\tilde{z}_t$  according to the weight ( $\tilde{w}_t^n$ ) with Equation (8).

**Step 5.** FOR  $i = 1 : n_p$  DO,

Normalize the particle weights as  $w_t^n = \tilde{w}_t^n / \sum_{n=1}^{n_p} \tilde{w}_t^n$ . The particles will then be retained according to their weights ( $w_t^n$ ) by the re-sampling process.

**Step 6.** Obtain the estimated target state by  $\bar{x}_t = \sum_{n=1}^{n_p} w_t^n \hat{x}_t^n$ .

**end**

### 3 EXPERIMENT AND DISCUSSION

#### 3.1 Specifications of APOSOS Telescope and Image Datasets

In our experiment, we used input images from two datasets of a real astronomical background, obtained by an APOSOS telescope on an alt/azimuth mount, equipped with a complementary metal-oxide semiconductor (CMOS)-type high-resolution sensor. These were stored as Flexible Image Transport System (FITS)-type grayscale images with range  $[0, 255]$ , 150-mm aperture size, 300-mm focal length and a  $3 \times 3$  degree<sup>2</sup> field of view. The observation site was located at National Astronomical Observatories, Chinese Academy of Sciences, Beijing, China (as identified by World Geodetic System 1984 (WGS84): Lat. 40.0028 and Long. 116.3876 degrees). For the telescope guidance system, the APOSOS telescope applied the orbit parameters of two line elements to calculate the orbital prediction. The datasets cover the two primary situations in space observation: normal-sky background composed of 43 frames, and a critically dynamic background consisting of 30 frames. These are labeled as datasets A and B, respectively, as shown in Figure 3.

**Table 1** Comparison of Optical Space Debris Extraction Algorithms

Optical space debris extraction algorithm via dataset A: normal-sky background																
Frame Index	SCRi	Median Image			Ng and Delp's method									RGA-Fuzzy		
					$\alpha = 0.25$			$\alpha = 0.50$			$\alpha = 0.75$					
		SCR	iSCR	BSF	SCR	iSCR	BSF	SCR	iSCR	BSF	SCR	iSCR	BSF	SCR	iSCR	BSF
1	0.901	1.069	1.186	1.504	3.608	4.004	0.946	3.961	4.396	0.946	3.481	3.862	0.946	3.971	4.406	1.504
5	5.119	5.758	1.125	0.771	8.025	1.567	1.375	9.548	1.865	1.064	7.539	1.147	0.880	8.078	1.578	1.001
10	10.645	12.516	1.176	1.139	5.016	0.471	1.120	5.323	0.500	0.839	5.0116	0.471	0.748	12.601	1.183	1.090
15	11.185	12.075	1.078	1.186	2.903	0.259	1.138	2.357	0.210	1.138	3.345	0.299	1.138	14.549	1.300	1.186
20	12.222	13.011	1.065	0.895	9.958	0.814	1.031	9.965	0.815	0.903	7.862	0.643	0.906	15.733	1.287	1.036
25	9.286	9.187	0.989	0.884	10.570	1.138	1.020	9.478	1.020	1.020	7.432	0.800	1.020	11.418	1.229	1.156
30	12.962	12.281	0.947	1.118	7.801	0.601	1.146	6.547	0.505	1.137	7.199	0.556	1.127	13.961	1.076	1.118
35	13.651	11.131	0.815	0.896	11.671	0.854	0.863	12.081	0.884	0.866	9.283	0.680	0.898	10.768	0.788	0.841
40	14.226	14.911	1.048	1.036	11.905	0.836	0.908	12.032	0.845	0.923	9.573	0.672	0.951	14.738	1.036	1.015
Average	9.977	10.215	1.048	1.047	7.934	1.172	1.061	7.921	1.227	0.982	6.747	1.050	0.957	11.757	1.543	1.105
Optical space debris extraction algorithm via dataset B: critically dynamic background																
Frame Index	SCRi	Median Image			Ng and Delp's method									RGA-Fuzzy		
					$\alpha = 0.25$			$\alpha = 0.50$			$\alpha = 0.75$					
		SCR	iSCR	BSF	SCR	iSCR	BSF	SCR	iSCR	BSF	SCR	iSCR	BSF	SCR	iSCR	BSF
1	0.120	0.147	1.225	0.483	0.149	1.241	0.413	0.146	1.216	0.393	0.152	1.266	0.516	0.156	1.301	0.483
5	0.591	0.263	0.445	0.484	1.321	2.235	0.260	1.915	3.240	0.233	1.911	3.233	0.285	1.718	2.906	0.768
10	1.629	0.609	0.373	0.471	0.853	0.523	0.349	1.794	1.101	0.207	2.214	1.359	0.239	2.271	1.393	1.103
15	2.406	1.151	0.478	0.320	1.783	0.741	0.300	3.112	1.293	0.250	3.896	1.619	0.313	4.255	1.768	0.320
20	1.229	1.023	0.832	0.283	1.365	1.110	0.773	1.825	1.484	0.777	2.214	1.801	0.971	2.481	2.018	0.361
25	1.846	1.062	0.575	0.339	1.172	0.634	0.410	1.776	0.962	0.587	2.031	1.099	0.513	2.171	1.176	0.339
30	2.625	0.083	0.031	0.563	1.104	0.420	0.402	1.832	0.697	0.294	1.972	0.751	0.520	1.831	0.697	0.649
Average	1.492	0.619	0.565	0.420	1.106	0.986	0.416	1.771	1.428	0.391	2.055	1.590	0.480	2.126	1.608	0.574

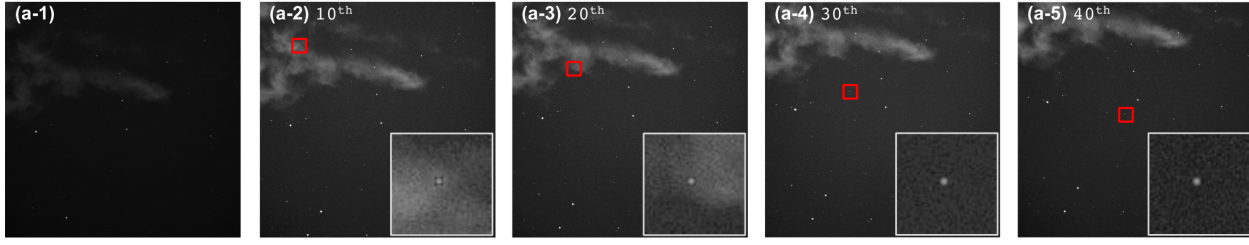
### 3.2 Performance Evaluation and Comparative Analysis

The background clutter is typically non-Gaussian and independent both pixel to pixel and frame to frame, which can be observed from  $\sigma_{\text{bk}}^{\text{ROI}}$ , as shown in Figure 4(b) and (d). Moreover, this parameter is inversely proportional to the extraction performance. The first experiment is related to the object-extraction procedure, which follows the updating process of the adaptive background model based on the human visual interpretation method proposed by Ng & Delp (2010). This method was applied in indoor environments, and it uses  $\alpha$  in order to balance the effects of  $I_t^{(x,y)}$  and  $\delta_{t-1}^{(x,y)}$ . Normally, the user adjusts  $\alpha$  from stability to rapid-update rate by following two main conditions, which are the illumination and object movement, based on specific experience. Therefore, the performance of moving-object extraction depends on selection of the optimal value of  $\alpha$ . In this work, following the concept of Ng and Delp's method, an updating process can be divided into three primary conditions: stability, equilibrium and rapid update, which are defined by

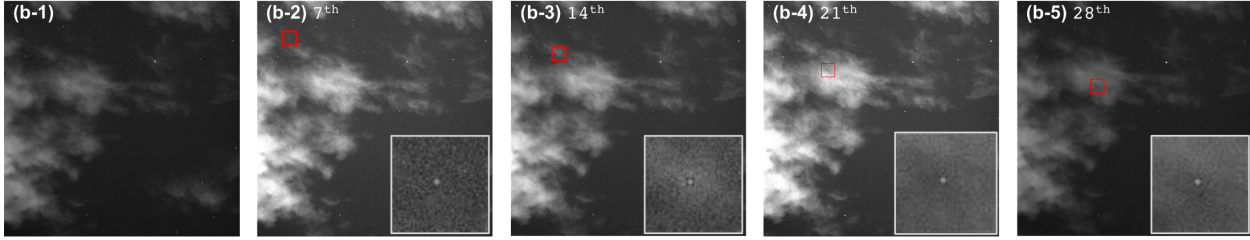
fixed values of  $\alpha = 0.25, 0.5$  and  $0.75$ , respectively, as illustrated in Figure 4(a) and (c).

From statistical data in Table 1, in the case of dataset A (normal-sky background), the illumination change is relatively stable; therefore, the object is extracted by a value of  $\alpha$  selected between the stability and equilibrium conditions ( $\alpha \in [0.25, 0.5]$ ). Consequently, the average of output SCR values, which are 7.934 and 7.921, can be achieved. However, in case of dataset B (critically dynamic background), noise is non-Gaussian and dynamically changes from frame to frame. The update condition that should be followed is  $I_t^{(x,y)}$  rapidly ( $\alpha \rightarrow 0.75$ ), which can identify the moving object with higher average of output for SCR when compared to the two other conditions with 2.055.

However, the situation is different when considering space debris observation and observation in an indoor environment because we cannot control the illumination in the former type of observation. Moreover, the atmospheric effects are normally unpredictable. Thus, the selected value of  $\alpha$  can be changed with observation time. It is complicated to interrupt the process to adjust the



(a) Dataset A. Normal-sky background.



(b) Dataset B. Critically dynamic background.

**Fig. 3** (a-1) and (b-1) Astronomical background model established from 10 frames. (a-2)–(a-5) and (b-2)–(b-5) are the moving space debris in dataset A and dataset B, respectively. The red rectangles mark the observation with a  $64 \times 64$  pixel<sup>2</sup> ROI around the space debris. The PSF of the moving space debris is shown at the bottom right of the image sequence.

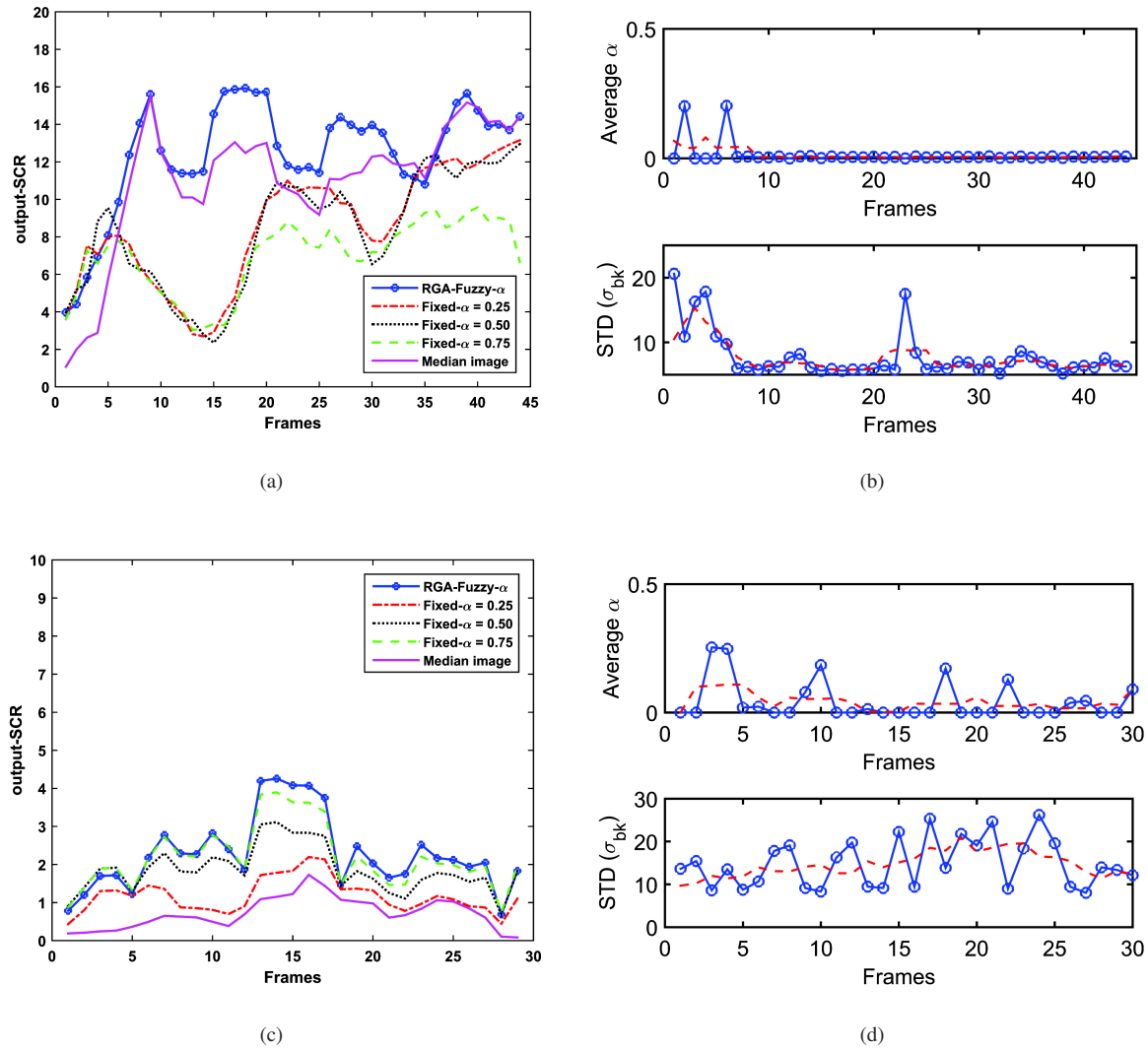
parameter  $\alpha$ . Therefore, an astronomer usually performs observations under clear-sky conditions and extracts the moving object by using the median technique. However, from human visual interpretation, as mentioned above, a learning process can be set up for intelligent fuzzy conditions.

Figure 4(b) shows the fuzzy  $\alpha$  and  $\sigma_{\text{bk}}^{\text{ROI}}$  of dataset A. The fuzzy  $\alpha$  is consequently assigned to  $\delta_{t-1}^{(x,y)}$  with a background model that is recursively updated twice. In dataset B, as shown in Figure 2(b), the critical dynamics of the atmospheric effects cause the fuzzy  $\alpha$  to be assigned to  $I_t^{(x,y)}$  with a background model that is recursively updated multiple times. Figure 4(a) and (c) compares the extraction algorithms in terms of the output SCR.

The extraction performance is measured by the improved-SCR (iSCR), which represents the enhancement in the extraction procedure with  $\text{SCR}_i$  before and after being processed with the output SCR, and the background suppression factor (BSF), as illustrated in Table 1. The results clearly demonstrate that the RGA-Fuzzy approach outperforms the median technique under the condition of a dynamic background. The average output SCR of the median and RGA-Fuzzy approaches are 10.215 and 11.757 for dataset A, and 0.619 and 2.126 for dataset B, respectively.

In the second experiment, to evaluate the tracking performance, a moving object based on the dead-reckoning approach was used to generate the path of space debris in 2D spatial coordinates using two real datasets. We assumed that a single moving object of space debris appeared to cover the whole image sequence with a constant velocity and crossed over the critically dynamic background area, as illustrated for dataset B in Figure 3(b-2)–(b-5). We used the Tycho-2 star catalog to identify fixed stars as reference positions and transform the estimated position in 2D spatial coordinates to celestial coordinates based on the least-squares method (Kovalevsky & Seidelmann 2004). The fixed reference stars were then recognized by  $\delta_N^{(x,y)}$ . The tracking performance with the proposed method was evaluated in terms of accuracy and robustness, and compared with two combination algorithms: median PF-TBD and RGA-Fuzzy PF-TBD.

In the simulation process, PF-TBD worked with the optimal number of particles,  $n_p = 975$ . Uniform proposal densities for the particles were defined as  $x_{p_t}^{(x,y)} \sim \rho(-5, 5)$ ,  $x_{v_t}^{(x,y)} \sim \rho(-1, 1)$  and  $x_{\tau_t} \sim \rho(-5, 2)$ , with the probability of target existence  $P_b = P_d = 0.01$ . The initial state vector of space debris was  $x_{(t=0)} = [80, 10, 924, -10, 15]^T$  with SNR  $\approx 5.97$  dB. Tracking was conducted with an observation size of  $\Delta_x = \Delta_y =$



**Fig. 4** (a) and (c) Comparison of the extraction performance with datasets A and B, respectively. (b) and (d) Average of fuzzy  $\alpha$  based on the second condition of Eq. (2) (*top*) and STD in a specific ROI (*bottom*) corresponding to datasets A and B, respectively.

5. The tracking accuracy was measured as the root-mean-square error (RMSE) between the true and estimated positions. In the first tracking validation, we employed dataset A, which is a common scenario in a low-clutter background. It includes a partly cloudy background in the first ten frames, as illustrated by the STD clutter level in Figure 4(b). The tracking performance achieved using this dataset is shown in Figure 5(a). In a comparison using the average RMSE value and considering all of the tracking frames, the median PF-TBD and RGA-Fuzzy PF-TBD are 0.1801 degrees and 0.0807 degrees, respectively. In other words, RGA-Fuzzy PF-TBD reduces the tracking error by 26.8%. However, after the first ten frames of dataset A, both combination algorithms worked well on account of the low clutter ratio.

In the second tracking validation, we used dataset B. As shown in Figure 4(d), the fitted data (dashed line) exhibit an increasing STD clutter level. The object path is shown in Figure 4(c). It is evident that the static background model associated with the median technique works well at first; however, the SCR soon declines on account of the clutter signal, which causes the tracking result of median PF-TBD to be diverted. Nevertheless, in the case of RGA-Fuzzy PF-TBD, tracking continues under this condition with an average RMSE of 0.2529 degrees. To determine the robustness of the proposed approach, we did not adjust the PF-TBD parameters in the new environment. It is known that  $n_p$  selection is one of the important factors in PF-based object tracking. Although the

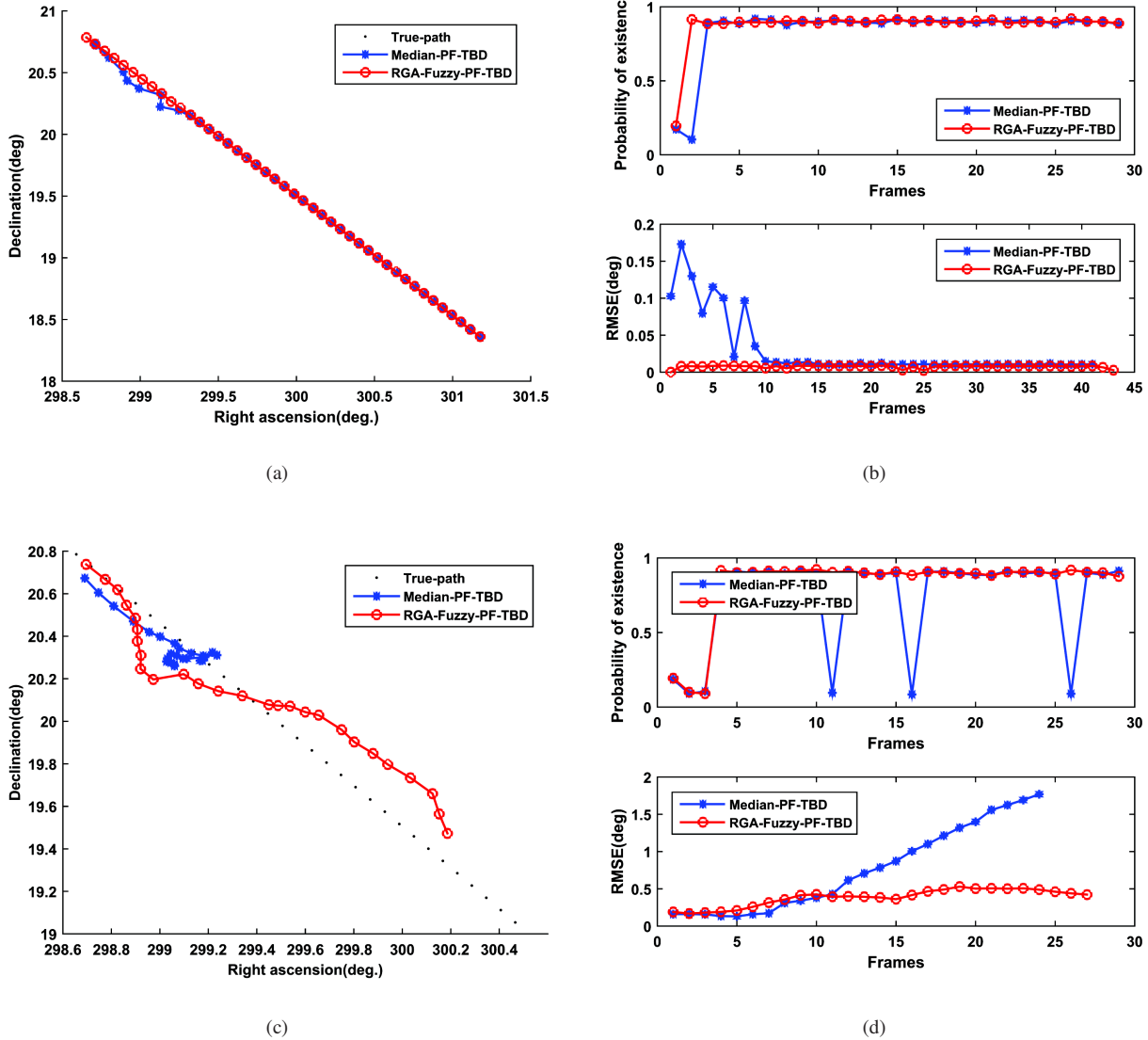


**Fig. 5** (a) and (c) Estimates of the positions of datasets A and B respectively given by two methods. (b) and (d) Probability of target existence (*top*) and RMSE (*bottom*) corresponding to datasets A and B, respectively.

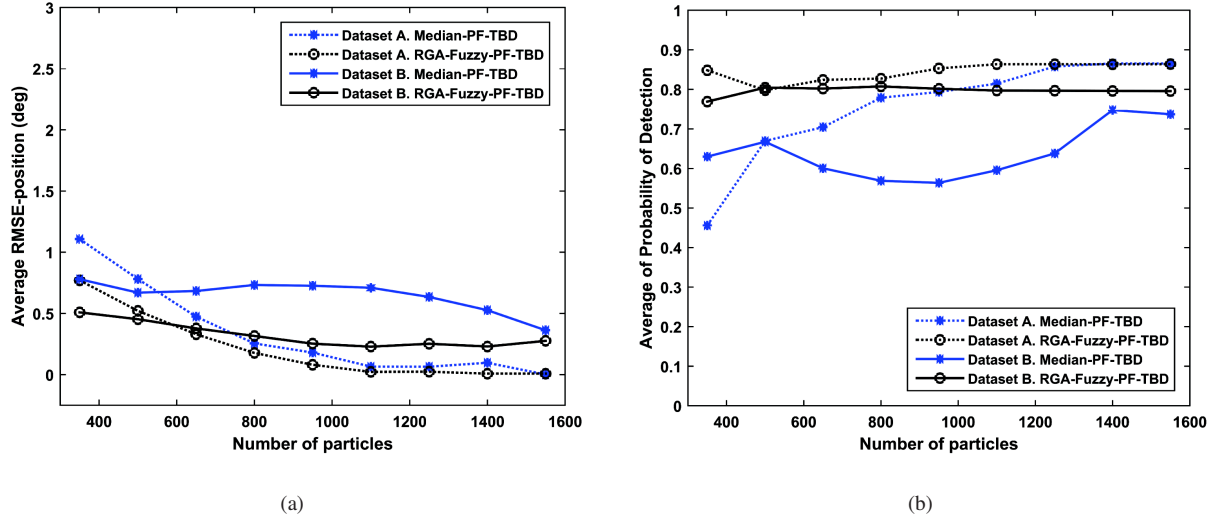
increase of  $n_p$  improves the accuracy and robustness of the algorithm, it is proportional to computation time.

Figure 6(a) shows the correlation between the linear increase of  $n_p \in [350, 1550]$  and pose-estimation accuracy. We observe that, although the performance difference between median PF-TBD and RGA-Fuzzy PF-TBD algorithms decreases exponentially as  $n_p$  increases, RGA-Fuzzy PF-TBD demonstrates a more consistent result compared to median PF-TBD. This indicates that the RGA-Fuzzy PF-TBD measure is less sensitive to  $n_p$  and hence a more robust measure in practice. In Figure 6(a) and (b), when  $n_p \in [800, 1000]$  for the proposed method,

both pose-estimation accuracy and detection sensitivity fall to the steady-state level with a slight improvement.

Therefore, in order to achieve a balance between tracking efficiency and accuracy, optical space-debris tracking with  $n_p \in [800, 1000]$  is optimal for implementation in this article. We also analyze detection and tracking performance under different levels of intensity.

Figure 7 shows the performance of the proposed algorithms for fixed  $n_p = 975$  with four levels of dim intensity,  $\text{SNR} = \{3, 6, 9, 12\}$  dB. It can be seen from Figure 7 that the position errors of both combination algorithms are inversely proportional to the intensity value.



**Fig. 6** (a) Pose-estimation accuracy for different numbers of particles. (b) Average detection sensitivity for different numbers of particles, corresponding to datasets A and B.

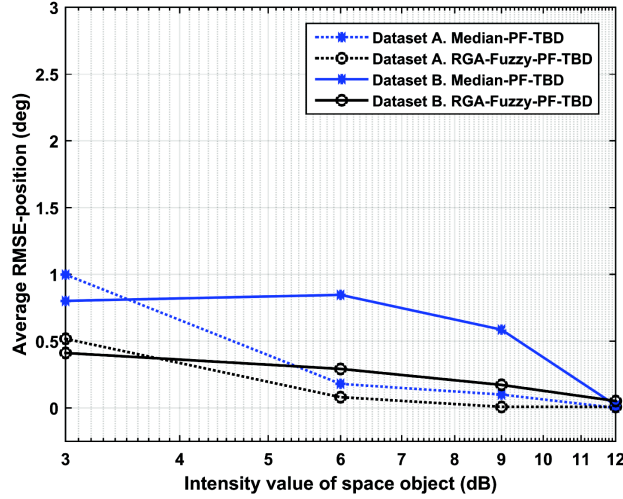


**Fig. 7** Pose-estimation accuracy for different intensity values of a space object with  $\text{SNR} = \{3, 6, 9, 12\}$  dB.

However, for intensity levels greater than 12 dB, both combination algorithms work well.

In other words, the position error will converge to zero when light scattered from the object can overcome background noise. When evaluating the performance of tracking small and dim targets, one indicator that is often used in the literature is the tracking amplitude error ( $\text{Amp}_{\text{err}}$ ), which is shown in Figure 8(a) and (b).

This parameter reflects the detection performance as a function of likelihood and can be expressed as follows

$$\text{Amp}_{\text{err}} = \sqrt{\frac{1}{L} \sum_{i=1}^L \|A_r - A_{\text{es}}\|_t^2}, \quad (9)$$

where  $L$  is the length of the track. The parameters  $A_r$  and  $A_{\text{es}}$  are the real amplitude and estimated amplitude in dB, respectively.

Note that both the bias and variance of the approximate tracking amplitude are considered in  $\text{Amp}_{\text{err}}$ .

Table 2 summarizes the amplitude error of the two combination algorithms with two types of datasets having multiple values of object intensity. We consider Figure 8 and Table 2 together with  $\sigma_{\text{bk}}^{\text{ROI}}$ , as shown in Figure 4(b) and (d). Consequently, the problem of tracking-amplitude fluctuation mainly comes from the variance of background noise. Considering the likelihood function in Equation (8), although accurate integration of

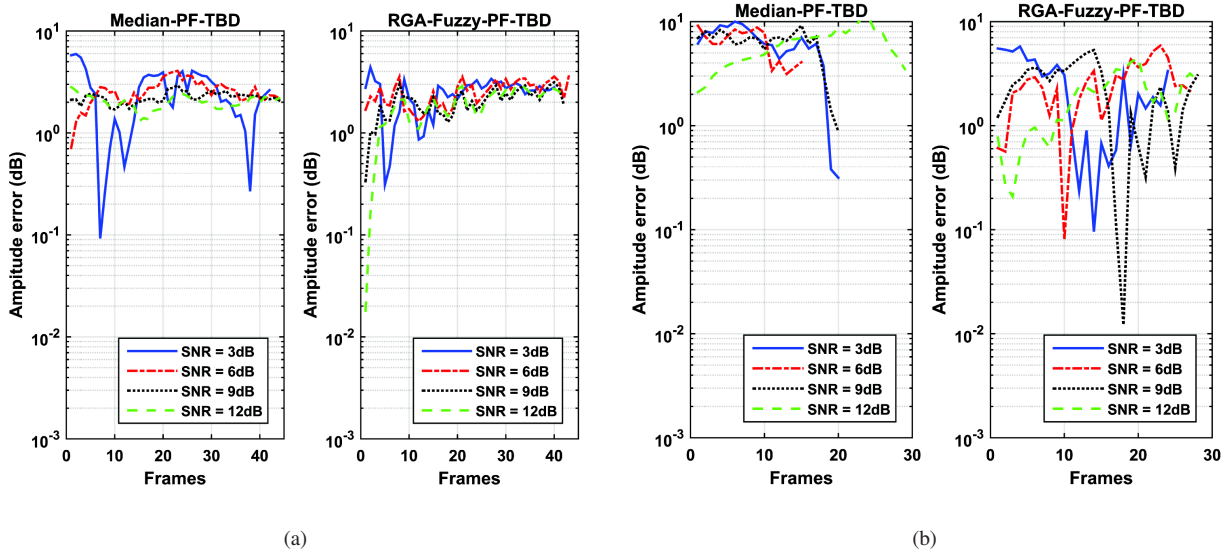


Fig. 8 (a) and (b) Comparison of average amplitude tracking error in dB between Median-PF-TBD and RGA-Fuzzy-PF-TBD for datasets A and B, respectively.

Table 2 Tracking Amplitude Error of Two Datasets for Different Intensity Values of a Space Debris Object

Dataset A. Normal-sky background												
Algorithms	Intensity value of space object											
	3dB			6dB			9dB			12dB		
	Min	Mean	Max	Min	Mean	Max	Min	Mean	Max	Min	Mean	Max
Median PF-TBD	0.092	2.513	5.941	0.714	2.564	4.065	1.699	2.235	2.942	1.303	2.009	2.813
RGA-Fuzzy PF-TBD	0.311	2.462	4.398	1.303	2.529	3.576	0.336	2.058	3.140	0.018	1.927	2.982
Dataset B. Critically dynamic background												
Algorithms	Intensity value of space object											
	3dB			6dB			9dB			12dB		
	Min	Mean	Max	Min	Mean	Max	Min	Mean	Max	Min	Mean	Max
Median PF-TBD	0.315	6.246	10.002	3.137	6.320	9.133	0.875	6.280	9.184	2.098	5.995	11.338
RGA-Fuzzy PF-TBD	0.095	2.548	5.767	0.079	2.552	5.885	0.012	2.367	5.332	0.207	1.904	4.476

the likelihood and median technique would slightly alleviate this problem, the majority of the effect is due to the considerable broadening of the likelihood function with respect to the target amplitude and nearest pixels of background noise. Normally, the boundary of the observation size should be defined in such a manner that the observation size is larger than the size of the object of interest. Consequently, a dim and small target will be affected more strongly, as illustrated in the statistical data in Table 2, which indicate that a dim target has a higher bias and STD of tracking amplitude error compared to a bright target. However, the proposed combination method can enhance the return amplitude of the

target with a bias lower than that resulting from combination with the median technique, which is an important value in the detection process.

#### 4 CONCLUSIONS

In this article, we have described a novel technique to solve the problem of tracking small and dim space debris under real dynamic and/or non-Gaussian backgrounds. The method includes two main steps. The first step is the extraction approach, in which we apply fuzzy logic to automatically estimate the optimal value of the empirical weight in traditional RGA. According to these re-

sults, this approach not only reduces the effect of the dynamic background, but also improves the extraction performance and robustness over those of the traditional median technique. We then integrate the first procedure with the second step, a PF-TBD approach. The results demonstrate that the proposed combination of algorithms provides considerable improvement in tracking accuracy, precision and robustness compared to other methods under dynamic real background noise. However, the shape of space debris that appears on the screen is only in the PSF. Therefore, the proposed method performs well with short exposure times.

**Acknowledgements** The authors are thankful for support from The World Academy of Sciences (TWAS), the Chinese Academy of Sciences (CAS), and the Asia-Pacific Space Cooperation Organization (APSCO). They are also grateful to the reviewers for their detailed reviews and constructive comments and suggestions. This work was supported as part of a national major scientific research equipment development project of China (No. ZDYZ2013-2).

## References

- Fujita, K., Hanada, T., Kitazawa, Y., & Kawabe, A. 2012, *Advances in Space Research*, 49, 1007
- Gao, H., & Li, J. 2014, *Sensors*, 14, 10829
- Hampf, D., Riede, W., Stöckle, G., & Buske, I. 2014, *Ground-Based Optical Position Measurements of Space Debris in Low Earth Orbits* (Deutsche Gesellschaft für Luft-und Raumfahrt-Lilienthal-Oberth eV)
- Karlin, S., Taylor, H. M., Karlin, S., & Taylor, H. M. 1998, *An Introduction to Stochastic Modeling*, Third Edition (Academic Press)
- Kovalevsky, J., & Seidelmann, P. K. 2004, *Fundamentals of Astrometry* (Cambridge: Cambridge University Press)
- Ng, K. K., & Delp, E. J. 2010, in *IS&T/SPIE Electronic Imaging*, International Society for Optics and Photonics, 75430M
- Raol, J. R. 2009, *Multi-Sensor Data Fusion with MATLAB®* (CRC Press)
- Ristic, B., Arulampalam, S., & Gordon, N. 2004, *Beyond the Kalman Filter: Particle Filters for Tracking Applications*, 685 (Artech House Boston)
- Salmond, D., & Birch, H. 2001, in *Proceedings of the American Control Conference*, 5, 3755
- Stoveken, E., & Schildknecht, T. 2005, in *Proceedings of the 4th European Conference on Space Debris*, Darmstadt, Germany, 18
- Sun, R.-Y., & Zhao, C.-Y. 2013, *RAA (Research in Astronomy and Astrophysics)*, 13, 604
- Wang, C., & Qin, S. 2015, *Infrared Physics and Technology*, 69, 123
- Ye, T., & Zhou, F. 2015, *Appl. Opt.*, 54, 3455